Electrochimica Acta 54 (2009) 6756–6766

Contents lists available at ScienceDirect

Electrochimica Acta

journal homepage: www.elsevier.com/locate/electacta

Enhanced activity and interfacial durability study of ultra low Pt based electrocatalysts prepared by ion beam assisted deposition (IBAD) method

N. Ramaswamy[a], T.M. Arruda[a], W. Wen[a,1], N. Hakim[a], M. Saha[a,2], A. Gullá[b], S. Mukerjee[a,*]

[a] Department of Chemistry and Chemical Biology, Northeastern University, 360 Huntington Avenue, Boston, MA 02115, USA
[b] De Nora R&D Division, 625 East Street, Fairport Harbor, OH 44077, USA

ARTICLE INFO

Article history:
Received 2 February 2009
Received in revised form 11 June 2009
Accepted 12 June 2009
Available online 23 June 2009

Keywords:
Low Pt loading
Dual IBAD
PEMFC durability
X-ray absorption spectroscopy
Oxygen reduction reaction

ABSTRACT

Ultra low loading noble metal (0.04–0.12 mg_{Pt}/cm^2) based electrodes were obtained by direct metallization of non-catalyzed gas diffusion layers via dual ion beam assisted deposition (IBAD) method. Fuel cell performance results reported earlier indicate significant improvements in terms of mass specific power density of 0.297 g_{Pt}/kW with 250 Å thick IBAD deposit (0.04 mg_{Pt}/cm^2 for a total MEA loading of 0.08 mg_{Pt}/cm^2) at 0.65 V in contrast to the state of the art power density of 1.18 g_{Pt}/kW using 1 $mg_{Pt(MEA)}/cm^2$ at 0.65 V. In this article we report the peroxide radical initiated attack of the membrane electrode assembly utilizing IBAD electrodes in comparison to commercially available E-TEK (now BASF Fuel Cell GmbH) electrodes and find the pathway of membrane degradation as well. A novel segmented fuel cell is used for this purpose to relate membrane degradation to peroxide generation at the electrode/electrolyte interface by means of systematic pre and post analyses of the membrane are presented. Also, we present the results of *in situ* X-ray absorption spectroscopy (XAS) experiments to elucidate the structure/property relationships of these electrodes that lead to superior performance in terms of gravimetric power density obtained during fuel cell operation.

1. Introduction

Proton exchange membrane fuel cells (PEMFCs) are highly attractive as alternative renewable energy sources for various applications such as consumer electronics, terrestrial-orbit missions, vehicular and automotive applications [1–4]. Among the various fuel cell technologies available, the growth of PEMFC has been very rapid in the last couple of decades almost completely eclipsing alkaline and phosphoric acid fuel cell technologies mainly due to low temperature operation, decreased Pt electrocatalyst loading, bifunctional properties of Pt based alloy electrocatalysts, and efficient proton transport using Nafion® membranes. Key components of PEMFC include membrane electrode assembly consisting of anode and cathode electrocatalysts, ion exchange membrane, and bipolar plates, etc. [5]. PEMFC's exhibiting high power densities and durability are already the state of the art thereby necessitating more research in reducing capital cost by shifting attention to judicious choice of materials and fabrication, and also by facilitating procedures for scale up. The bulk of the cost of components used in a PEMFC stack comprises of the membrane electrode assembly and in particular the electrocatalysts (supported Pt and Pt alloys) [6]. In this context cost reduction has been achieved through several approaches, such as reducing electrocatalyst loading by maximizing three phase reactant–electrode–electrolyte interface, thus leading to better electrocatalyst utilization. In the 1960s and 1970s exceptionally high loadings of 4–40 mg/cm^2 Pt and Pd black catalysts were utilized in making membrane electrode assemblies [4]. The introduction of high surface area carbon blacks for supporting precious metals have decreased the catalysts loading by ten to hundred orders of magnitude down to 0.4–0.5 mg/cm^2 loading [7]. Researchers at Los Alamos National Laboratory were able to decrease the cathode Pt loading down to 0.12 mg/cm^2 with no concomitant detrimental effect on fuel cell performance [8]. In parallel to this, efforts at Texas A&M University also exhibited great strides towards lowering Pt loadings as low as 0.05 mg/cm^2 with comparable performance to those previously reported with 5 mg/cm^2 [9].

In this context it is important to note that the current goal set by DOE aims for specific power (including area specific power) of 0.3–0.2 g (PGM[3])/kW or 0.3–0.2 $mgPt/cm^2$ (2010 leading to 2015 targets). Since the cost targets are \$5 and \$3/kW (2010 and 2015

* Corresponding author. Tel.: +1 617 373 2382; fax: +1 617 373 8949.
E-mail address: s.mukerjee@neu.edu (S. Mukerjee).
[1] Present address: Shanghai Synchrotron Light Source (SSRF), Shanghai, China.
[2] Present address: Dept. of Mechanical and Materials Engg., University of Western Ontario, Ontario, Canada.

[3] PGM: Pt group metals.

0013-4686/$ – see front matter © 2009 Published by Elsevier Ltd.
doi:10.1016/j.electacta.2009.06.040

targets), an even more ambitious target may be needed depending on the increase in cost of Pt (currently priced at $1300/ounce[4]) From an automotive perspective a prior review by Gasteiger et al. [6] have pointed out that for automotive application the current state of the art (with H_2/Air at 80 °C), which is at approximately 0.7 W/cm^2 at 0.68 V (for 58% energy conversion) corresponding to 0.85–1.1 g_{Pt}/kW requires to transition to 0.2 g_{Pt}/kW at ≥0.65 V. Translating to the current DOE targets for 2010 leading to 2015 is 0.44 A/mgPt or 720 μA/cm^2 @ 900 $mV_{iR\,free}$. This can be envisaged as a dual effort wherein (a) MEA power density is improved to 0.8–0.9 W/cm$^2{}_{MEA}$ at ≥0.65 V by increasing Pt utilization and lowering mass transport and ohmic contributions and (b) increasing the inherent activities of the reaction zone by changing the nature of the conventional supported Pt electrocatalysts (Pt nanoparticles) via means such as alloying and modification of surface morphology. In this context it is important to note that the noble metal loading at the anode can be reduced from the current loadings of 0.2–0.4 to 0.05 $mg_{Pt(MEA)}$/cm^2 without concomitant losses at the anode [10]. Hence the principal focus in this context involves the cathode electrode. In this context the issue of mass manufacturability with simultaneous control on reproducibility and cost minimization has also been addressed. There have been several efforts towards lowering of noble metal loading which are classified into four broad categories based on the deposition methods used: (i) thin film formation with carbon supported electrocatalysts, (ii) pulse electrodeposition of noble metals (Pt and Pt alloys), (iii) sputter deposition, and (iv) ion-beam deposition. A more detailed explanation of all these methodologies has been reviewed earlier by us [11]. The essence of these technologies is summarized here.

Widely practiced thin film formation methodology is the so called 'decal' approach in which a thin layer of supported electrocatalyst applied onto a Teflon blank is then transferred directly onto the membrane by hot pressing [12,13]. It is the objective of this methodology to extend the reaction zone further into the electrode layer away from the membrane. This ensures a more three dimensional structure to the membrane electrode assembly. Many variations to this method can be found in the literature [14–21]. Pulse electrodeposition involves the electrolytic deposition of Pt electrocatalysts from its salt solutions which relied on their diffusion through the thin Nafion® layer on carbon supports [22,23]. Electrodeposited Pt electrodes are expected to exhibit higher utilization efficiency since theoretically deposition takes place at the most energetically favorable zones [24,25]. Sputter deposition is another method [26–29], in which the noble metal catalyst is deposited on carbon diffusion electrode, here however the interfacial reaction zone is at the frontal surface with the membrane. Although sputter deposited Pt electrocatalysts with loading as low as 0.01 mg_{Pt}/cm^2 shows equivalent performance to that of the conventional Pt/C (0.4 mg_{Pt}/cm^2), the generic problem has been the durability and the electrode more prone towards dissolution and sintering of the deposits.

Ion-beam technology, the methodology used in this research effort offers various advantages over the earlier described techniques where the benefits of low energy ion bombardment along with the thin film vacuum deposition process is exploited to for obtaining dense, adhering and robust depositions. For recent reviews and modifications of this approach the readers are referred to the references [30–32]. Noble metal electrodes manufactured by Ion Beam Assisted Deposition (IBAD) offers the following advantages: (i) better utilization efficiency of the precious metal present on the electrode in PEMFCs, (ii) very low precious metal loading, (iii) low temperature methodology which is very easy to scale up, (iv) produces a catalyst layer entirely composed of nanoparticles/nanocrystalline thin films with control over size and distribution while eliminating the need for dispersing/supporting medium and also the interfacial Nafion® ionomer layer between the electrode and membrane electrolyte. More details about the preparation methodology of the IBAD electrodes are given in our previous publication [11].

In our previous publications [11,33,34], dual IBAD was successfully used to prepare ultra-low Pt loaded gas diffusion electrodes for PEMFC's with the principal advantages of higher mass specific power density (mg_{Pt}/kW) combined with the mass manufacturability. Two ion beams were used, one to roughen the substrate and the other to embed the target atoms (Pt or an additional transition metal in this case). The morphologies obtained are very different from the conventional Pt/C electrocatalyst. Ultralow Pt loadings of the order of 0.04–0.12 mg/cm^2 were produced. Results indicated no change in ORR activation polarization [11], instead the overpotential followed the expected shifts based on Pt loading. More importantly, a mass specific power density of 0.297 g_{Pt}/kW was possible with an ultra low loading IBAD electrode containing 250 Å deposit (0.04 mg_{Pt}/cm^2 for a total MEA loading of 0.08 mg_{Pt}/cm^2). Among the three different IBAD electrodes reported earlier [11] (ranging from 750 to 250 Å deposit corresponding to 0.12–0.04 mg_{Pt}/cm^2), the mass specific power density variations were 0.29–0.55 g_{Pt}/kW. All these power density comparisons are predicated on a fixed potential of 0.65 V. This is contrasted with the commercial MEA with a loading of 1 $mg_{Pt(MEA)}$/cm^2 where mass specific power density obtained was 1.18 g_{Pt}/kW, a value typical of current state of the art commercial electrodes containing Pt/C. Considering the need to transition from the current state of the art towards a target of 0.2 g_{Pt}/kW, this is a good step forward. These performances were noteworthy considering there was no ionomer added to the IBAD layer deposited on a commercial non-catalyzed gas diffusion layer (GDL) (BASF fuel cells, LT1400). However, the principal shortcoming of this effort is the area specific power density which is in the range of 0.27–0.43 W/cm^2 at 0.65 V, hence much below the target value of 0.8–0.9 W/cm^2 (at 0.65 V). The principal cause of this lower area specific power density is the higher mass transport losses (see ref. [11] for details).

As a further development, our prior efforts also involved using dual ion beam assisted deposition to successfully prepare layered metal electrodes for PEMFCs. The first layer was either Co or Cr while the second layer was pure Pt [33]. The morphology of the deposits is very different from those typically encountered in carbon supported Pt electrocatalysts, both from the perspective of the relative population of the surface crystalline planes as well as particle size distribution. When compared to the standard IBAD prepared electrodes, the overall fuel cell performance was enhanced thus mimicking the same effect observable when a carbon supported alloy is prepared according to conventional means. In this rendition of the dual IBAD approach [33], two ion beams were used; one to roughen the substrate and the other to embed the target atoms (Pt, Co and Cr sequentially). Some differences were observed in the onset potential of CO_{ads} stripping which could be correlated with changes in crystalline nature of the deposit as well as presence of non-noble metal oxides. Of great importance was the fact that ORR activity was further enhanced as compared (for similar Pt loading) with no apparent evidence of alloying. Of particular significance arising out of the non-alloyed character of the Pt-M IBAD deposition was the fundamental question regarding true nature and characteristics required in the design of a "true" Pt based bimetallic catalyst and more importantly its durability at the interface with a polymer electrolyte membrane such as the prototypical Nafion® series (Dupont).

The objective of this report is to build on our previous reports [11,33–35] related to performance aspects of electrodes manufactured by ion beam assisted deposition technique by reporting

[4] Source Monex.com, Price as of 8/19/2008.

on its durability characteristics. These are reported from the perspective of (a) electrocatalyst stability, i.e., morphology changes and element specific corrosion measured *in situ* under actual electrochemical operating conditions using synchrotron based X-ray absorption spectroscopy. In addition we also report results of interfacial membrane stability by examining membrane degradation using a unique accelerated durability test methodology in conjunction with a novel high throughput array electrode assembly setup [36,37]. As reported earlier [36,37], using a combination of independent measurements of peroxide yields (by RRDE) and membrane degradation determined using *ex situ* IR measurements, there is direct correlation arising from the concomitant free radical generation associated with peroxides at the interface [36].

2. Experimental

Dual IBAD is a vacuum deposition process that combines physical vapor deposition (PVD) with ion beam bombardment. Vapors of coating atoms are generated with an electron beam evaporator and deposited on a substrate. Ions are simultaneously extracted from the plasma and accelerated into the growing PVD film at energies of several hundred to several thousand electron volts (500–2000 eV). Ion bombardment is the key factor controlling film properties in the IBAD process; thus imparting substantial energy to the coating and coating/substrate interface. This achieves the benefits of substrate heating without degrading its bulk properties. The major parameters are the coating material, evaporation rate, ion species, ion energy, and ion beam and current density; the influence of all these parameters are described in detail elsewhere [38,39]. In this work, dual IBAD was used directly to deposit two distinct metal layers onto a commercially available non-catalyzed GDL (LT1400-W, E-TEK BASF). The first metal layer was comprised of Co whereas the second metal was pure Pt deposited directly on top of the first metal layer. This electrode is named as bimetallic IBAD CoPt. A similar IBAD electrode was prepared by directly depositing Pt on GDL which is hereafter mentioned as IBAD Pt. All layers deposited had a pre-chosen thickness of 500 Å thus giving a total precious metal loading of about 0.08 mg/cm^2. The thicknesses of all the electrodes prepared were measured by analyzing a reference Si wafer coupon which was strategically located with the roll of carbon cloth during the deposition process. A profilometer was used to measure the thickness of the deposit on the Si wafer. This served as a direct correlation of deposition thickness on the GDL. The loadings were additionally measured by analyzing a statistically significant number of samples of known geometric area with the aid of the standard thermogravimetric analysis method. This allowed for a sensitive measurement of the effective loading of each sample, found to be within a 10% margin of error. Comparison was made with respect to the commercially available supported Pt/C electrodes with a metal loading of 0.5 mg/cm^2 (E-TEK, Somerset, NJ).

2.1. Electrochemical characterization

All electrochemical measurements were made at room temperature using a special electrochemical cell as described elsewhere [40], connected to an Autolab (Ecochemie Inc., model – PGSTAT 30) potentiostat equipped with a bi-potentiostat interface. All potentials in acidic and alkaline solutions were measured with respect to sealed hydrogen electrode (RHE) and Hg/HgO reference electrode respectively. De-oxygenated 1 M $HClO_4$, 1 M KOH were used as the electrolytes and a scan rate of 10 mV/s was utilized.

2.2. Segmented cell design

Durability experiments were performed using a modified fuel cell hardware based on a "high throughput screening fuel cell assembly" (NuVant System, Inc., IL, USA) [41]. Fig. 1a shows the original schematic of the fuel cell assembly. Its key components include an electronically conducting flow field block and an electronically insulating array block on the opposite side of the MEA. The array block has 25 sensors glued into the block on the opposite side facing one of the testing spots on the array MEA and a pin jack on the other side used for electrical connection. The heating control and gas supplies to this fuel cell were built in-house to enable the cell to run at ambient pressure and constant temperature up to 80 °C [42]. Gases were passed through humidification bottles, which were kept at a temperature 10 °C higher than that of the cell in order to ensure the 100% humidification of the MEA.

The MEAs in this work were customized for the purpose of the durability tests. As shown in Fig. 1b, the MEA consists of the membrane of interest with a size of 11 cm × 11 cm. Attached to one side of the membrane is a titanium mesh common counter electrode (CE). On the other side, the testing area of the MEA is divided into five testing units. Each unit has a strip of electrode as the working electrode (WE), and two disk electrodes for building the reference electrode (RE) of this unit. This design enables a simultaneous evaluation of five catalyst samples of geometric are 5 cm^2 (5 cm × 1 cm) at each run under same operating conditions. A

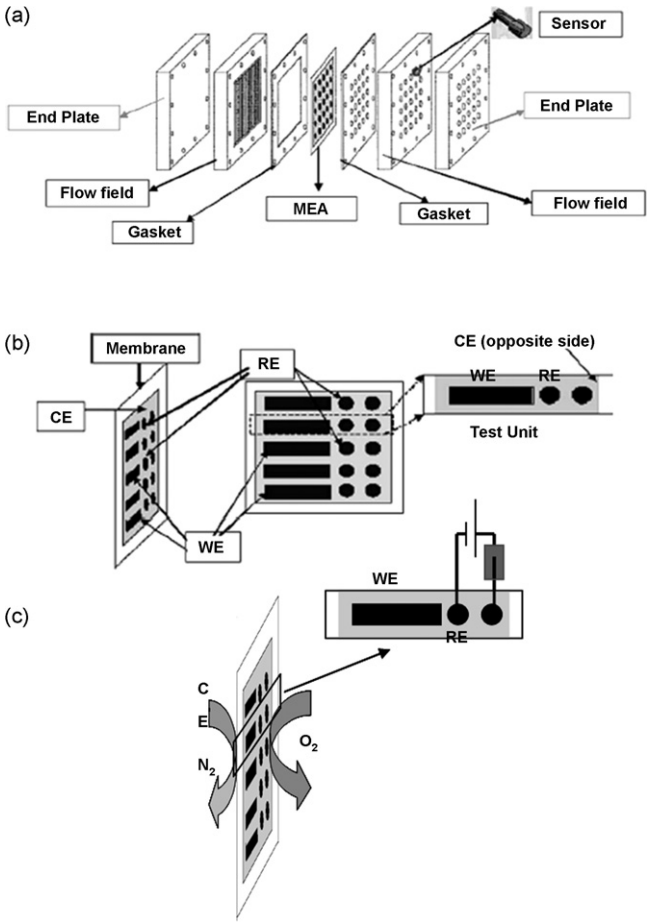

Fig. 1. (a) Segmented array fuel cell assembly designed for testing multiple working electrodes, each with individual reference electrodes and a common counter. (b) Design of MEA for durability test showing the five individual working electrodes (WEs) each with their reference electrode (RE) arrangement and common counter electrode (CE). (c) Schematic of the half cell arrangement for specifically mimicking cathode electrode interface degradation arising out of simultaneous peroxide generation during ORR. In this half cell mode counter electrode is in oxygen evolution mode providing the necessary protons for oxygen reduction at the WE. Note polarization is with respect to dynamic hydrogen electrode associated with each of the five separate WE's.

multi-channel Arbin (BT2000) Testing System (Arbin Instruments, TX) was used for polarization of the individual working electrodes.

2.2.1. Durability test design criteria

In prior publications concerning the susceptibility of PEM's to radical-initiated chemical attack, fuel cell experiments performed with either single cell or multi-cell stack played an important role. These extended life testing reflected indeed the combined impact from various sources (fuel cell component configuration, MEA fabrication, operating conditions, thermal and load cycles, impurities, and uniformity, etc.) on the lifetime of the membrane. However the interplay of these factors leads to inevitable difficulties in interpreting and reproducing the data and inability to assign the observed membrane failure to one particular factor without taking other possible triggers and/or enhancers into account. From this point of view, a unique membrane durability test involving a half cell configuration was designed so as to enable data interpretation. More details are given elsewhere [36]. Briefly, our cathode side durability test design involves, as shown in Fig. 1c, passage of humidified oxygen and nitrogen at ambient pressure as follows. Humidified oxygen is passed through the working electrode side of the cell; humidified nitrogen, which is inert therefore only functions to hydrate the MEA, is passed through the counter electrode side so that water molecules carried by nitrogen undergo oxidation at the counter electrode thus providing protons at the working electrode side purged with humidified oxygen. This design emulates an operating fuel cell except for eliminating hydrogen as a possible cause of peroxide formation. The reference electrode used was a solid-state dynamic hydrogen electrode (DHE) [43], which is constructed by connecting two disk electrodes (E-TEK 30% Pt/C electrode) to power supply of 1.7 V. After full hydration of the MEA, the potential of the working electrode could be set (vs. DHE) for 24–48 h time period at different potentials. Cathode side membrane degradation was studied both at normal fuel cell cathode operating potentials of 0.6 and 0.7 V vs. DHE and also accelerated conditions of membrane degradation was achieved at a cathode potential of 0.4 V vs. DHE in this present study. Pre- and post-test analysis of the membrane in contact with the working electrode is conducted. The results were then compared with the corresponding properties of the pure Nafion® membrane [Initial Conductivity = 0.1 S cm^{-1}, Ion Exchange Capacity = 0.91 mEq g^{-1}]. This design is based on the recent publications [44–49] which suggested that the vulnerable location for radical attack in a MEA is at the cathode (oxygen) side. This mechanism is based on the proposition of oxygen reduction reaction (ORR) at the cathode of PEMFC proceeding via a parallel pathway where a two-electron reduction of oxygen occurs simultaneously with the formation of H_2O_2 intermediates along with the predominant four electron reduction to H_2O; the peroxides then react with trace transition metals ions (Fe^{2+}, Cu^{2+}... found in membrane and/or carbon black catalysts support, fuel cell end plates) to form radicals. It has been pointed out that the metal ion and H_2O_2 concentrations necessary for the occurrence of hydroxyl radical can be very low (<10–25 mg L^{-1} H_2O_2 and 1 part Fe per 5–25 parts of H_2O_2 (wt/wt) [50,51]).

2.2.2. MEA fabrication for single cell and durability tests

For single cell measurements, MEA was fabricated using Nafion® 112 (DuPont) as the membrane. Membranes were cleaned in boiling 3% H_2O_2 for 1 h, 1 M H_2SO_4 for 1 h and rinsed in boiling deionized water at least twice (1 h). Electrodes and membrane were assembled and hot pressed at 125 °C for 5–10 min and 125–250 psig. Contrary to the conventional MEA assemblies, no extra liquid ionomer was used in the MEA fabrication involving IBAD electrodes.

For segmented cell experiments, working electrodes were selected from commercial E-TEK 30% Pt/C, IBAD 550 Å Pt and 550 Å PtCo (typical metal loadings of 0.08 mg/cm^2). Material for the reference electrode was 30% Pt/C electrode (E-TEK-BASF) with a metal loading of 0.5 mg/cm^2. For the cathode degradation test 0.6 mg_{Pt}/cm^2 of 80% Pt/C (E-TEK-BASF) was used as the counter electrode catalyst and titanium mesh for current collection. No liquid ionomer loading on IBAD electrodes were applied, whereas 0.8 mg/cm^2 of 5 wt% Nafion solution (Ion Power, Inc.) was applied on E-TEK Pt/C electrode.

2.2.3. Membrane characterization techniques

After the durability experiment, the MEA was uninstalled from the cell, and the working electrode portions were carefully cut off from the MEA with the appropriate working electrode side carefully labeled. The samples were then dipped in anhydrous methanol for a short fraction of a second to enable peeling of the electrodes from the membrane. The membrane samples so obtained, typically 1 cm × 5 cm, were then washed thoroughly with deionized water before performing the following analysis.

2.2.4. Fourier-transform infrared spectroscopy

Fourier transform infrared spectroscopy (FTIR) is a handy, non-destructive technique to probe changes in membrane chemistry due to degradation, used in numerous studies [52,53] and to determine the microstructure of Nafion® in prior PEM stability studies [54,55]. In this work, infrared spectra, plays an important role in revealing the chemical processes underlying degradation. Due to the thickness of the sample, attenuated total reflection (ATR) mode was employed instead of transmission mode. IR spectra were recorded with either Mattson RS-2 FTIR instrument equipped with a pike MIRacle ATR unit with 45° ZnSe ATR Crystal or Bio-Rad FTS6000 FTIR instrument with 45° Ge ATR crystal. The reason for using two different crystals is to exploit the difference in IR penetration depth that they provide due to difference in refractive index of ZnSe and Ge. ZnSe provides a penetration depth of 1.7–2 μm from the membrane surface whereas Ge has only 0.65–0.7 μm from the membrane surface [56]. For measurement, the dried sample (24 h in vacuum at 60 °C) was pressed against the ATR crystal with the help of a force-sensing pressure applicator. All spectra were collected from 400 scans at 4-cm^{-1} resolution. Dry nitrogen gas was purged around the sample during the measurement to eliminate moisture in the air. Linear background correction in the spectra was attained manually.

2.2.5. Conductivity measurement

Proton conductivity was determined from a fully humidified membrane at room temperature using four-probe conductivity cell setup described in our prior publication [57]. Measurements were carried out with a digital potentiostat/galvanostat (AUTOLAB model PGSTAT30 equipped with FRA model, Ecochemie B.V.).

2.2.6. Ion exchange capacity (IEC)

Ion exchange capacity defined as the ratio of moles of sulfonate ion exchange sites to the dry of Nafion® is expressed in mEq/g and were measured using standard methods, which involved equilibrating known amount of H^+ form of the membrane in measured volume of a standard solution of 3 M NaCl at 100 °C for 10 h to allow for the exchange with H^+ ions. This solution was then titrated to a phenolphthalein end-point with a standard NaOH solution.

2.2.7. In situ XAS data collection and analysis

All XAS experiments were conducted at room temperature utilizing *in situ* spectro-electrochemical cells described previously [58]. Each cell consisted of a 5 cm^2 working electrode (IBAD PtCo, or E-TEK 30% PtCo/C), counter electrode (washed in 0.5 M H_2SO_4 Grafoil®) and reference hydrogen electrode (RHE). The cells were configured by separating the WE and CE by a piece of Nafion® 112 (Du Pont Fluoroproducts) polymer electrolyte membrane. Au wire

(99.999%, Alfa Aesar) current collectors were mechanically pressed against the back side of each electrode. In all experiments the cells were flooded with purified [59] 1 M trifluoromethanesulfonic acid (TFMSA) electrolyte. For experiments utilizing E-TEK PtCo/C, electrodes were prepared from inks of the catalyst powder were hand painted onto gas diffusion electrodes (ELAT V2, E-TEK) until a loading of ~0.5 mg/cm^2 Co was achieved. The inks were made by combining the catalyst powder with 1:1 mixture of D.I. H_2O/2-propanol (wt/wt) and 5% Nafion® in lower alcohols (Ion Power, INC.). The cells were potentiostatically controlled by an Autolab® potentiostat (model PGSTAT30, Ecochemie-Brinkmann) interfaced to a laptop computer.

XAS measurements were made in fluorescence mode by placing the cell between two gas ionization detectors and collecting fluorescent X-rays at 90° to the incident beam with a 13 element Ge solid state detector. To correct for changes in the incident beam, reference scans were taken by placing a foil (Co or Pt) between the second and third gas ionization detectors for all measurements. Full range EXAFS measurements were collected (−200 eV to 16k) while potentiostatically controlling the WE at a single fixed potential for the duration of the EXAFS scan. The XAS data was analyzed using the IFEFFIT suite [60] (version 1.2.8, IFEFFIT Copyright 2005, Matthew Newville, University of Chicago, http://cars9.uchicago.edu/ifeffit/), which employs the AUTOBK algorithm [61] for background subtraction.

3. Results and discussions

3.1. Electrochemical characterization

IBAD Pt and PtCo electrodes (see experimental details on metal deposit thickness, loading, etc.) were characterized in a specially designed cell to investigate its surface electrochemical properties. This cell allowed for efficient mounting of the IBAD electrode with flow through sealed electrolyte chamber enabling de-oxygenated electrolyte to be circulated in conjunction with a counter (Grafoil®) and reference electrode (Hg/HgO which is 0.926 V vs. RHE). Fig. 2 shows the cyclic voltammogram obtained in de-oxygenated 1 M KOH electrolyte at 10 mV/s scan rate. Based on Pourbaix diagram and previous detailed electrochemical studies on Co surfaces [62,63] the following peak identifications are acquired. The peak at 0.15 V vs. Hg/HgO reference electrode in the IBAD Co–Pt bimetallic electrode correspond to the changes in surface cobalt oxidation from Co_3O_4 (mixed oxides comprising of CoO and Co_2O_3) to CoOOH with the corresponding surface Co oxide reduction peaks (cathodic scan) at −0.15 V vs. Hg/HgO. The oxidation/reduction peaks at −0.15 V/−0.35 V vs. Hg/HgO electrode correspond to the Pt oxide formation and reduction in PtCo (IBAD). From these results it is observed that Pt oxide formation and reduction are shifted cathodic in the bimetallic PtCo (IBAD) electrode compared to IBAD Pt/C. (An approximate cathodic shift of 0.25 V of Pt reduction peak in the case of Co–Pt IBAD electrode.) It is observed that there is considerable amount of cobalt present on the surface in the alloy electrode and also both Pt and Co exhibit elemental features on the surface indicate that there is a significant amount of Pt and Co islands present on the bimetallic PtCo (IBAD) electrode surface rather than being perfectly layered.

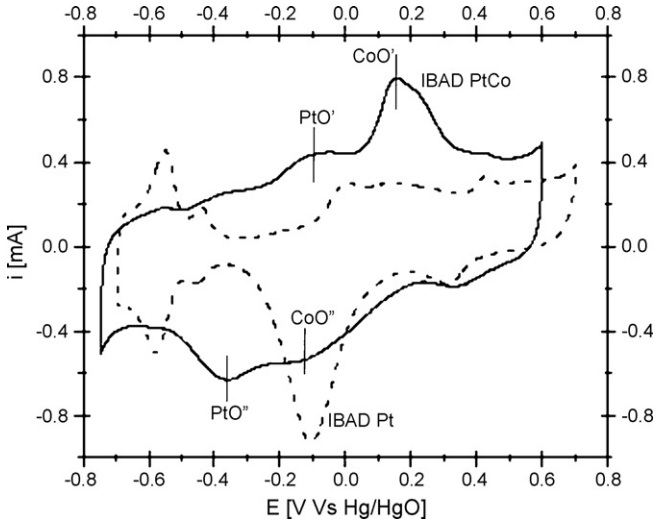

Fig. 2. Cyclic voltammetric curves for IBAD Pt (dashed line) and PtCo (solid line) GDEs in deareated 1 M KOH solution. Scan rate is 10 mV/s. In the case of IBAD PtCo electrode (solid line), single prime (′) indicates anodic oxide formation and double prime (″) indicates cathodic oxide reduction.

3.2. IBAD electrodes performance in single cell

Detailed analysis of fuel cell activity of IBAD electrodes is available elsewhere [11,33]; briefly its performance is summarized here. The precious metal loadings (Pt) of the IBAD electrodes used on the cathode side correspond to 0.08 mg_{Pt}/cm^2 (or 550 Å deposit) which is approximately four to five times lower loading compared to conventional carbon supported platinum electrocatalysts. Also in an earlier report [11,33,34], it was shown/that the presence of interfacial Nafion® ionomer layer between the electrode and membrane in MEA's consisting of IBAD electrodes lead to significant mass transport limitations (in quantitative terms, IBAD electrodes at a polarization potential of 0.7 V cell performance obtained was 430 mA/cm^2 without ionomer layer compared to 180 mA/cm^2 with ionomer layer yielding an improvement of 250 mA/cm^2 at 0.7 V) in contrast to conventional E-TEK Pt/C electrodes. Fuel cell polarization curves and Tafel plots of the IBAD Pt and Pt alloy electrodes in comparison to commercially available standard E-TEK Pt obtained at 80 °C, 50/60 psig back-pressure for anode and cathode electrodes respectively (100% humidification condition) with H_2/O_2 are shown in Fig. 3a and b. Electro-kinetic parameters derived from polarization curves are shown in Table 1. In the activation-controlled region, IBAD Pt-alloy electrodes show better performance than IBAD Pt electrode especially in the low current density activation-controlled region. For the MEA made with IBAD Co–Pt electrode, the fuel cell performance at 0.8 V is 0.24 and 0.48 A/cm^2 in H_2/air and H_2/O_2, respectively, with a total Pt loading of 0.16 mg_{Pt}/cm^2 per MEA (0.08/0.08 mg_{Pt}/cm^2 anode/cathode loadings), the resulting power densities are ca. 0.20 and 0.38 W/cm^2. Under conditions of H_2/air feed at 80 °C, the MEA prepared with Pt IBAD electrode resulted in a power density of 0.327 W/cm^2 at 0.65 V, translating into a Pt-specific power density of 0.734 g_{Pt}/kW. Hence while the area specific power density is lower, the gravimetric power density is a significant improvement as required for automotive

Table 1
Electrode kinetic parameters for IBAD Pt and Pt-M bimetallic electrodes measured in a 5 cm^2 single cell in conjunction with built in reference electrodes (RHE). Shown are the experimentally measured rest potential, Tafel slope, current density for the cathode electrode in the activation-controlled region (0.9 V vs. RHE) expressed in terms of geometric and gravimetric (mg-Pt) basis.

Electrode	E_o [mV]	Tafel Slope, b [mV/decade]	$I_{900\,mV}$ [mA/cm^2]	$I_{900\,mV}$ (mA/mgPt)
IBAD Pt	1009	68.5	59.8	747.8
IBAD CoPt	1023	61.4	98.8	1235.2
IBAD CrPt	1026	64.6	87.0	1087.8
ETEK-BASF Pt	1021	56.8	135.2	270.4

These data were obtained under operating condition of 80 °C, 50/60 psig back-pressure (anode and cathode electrodes respectively). Results are compared to a standard Pt/C (ETEK) electrode (0.5 mg/cm^2).

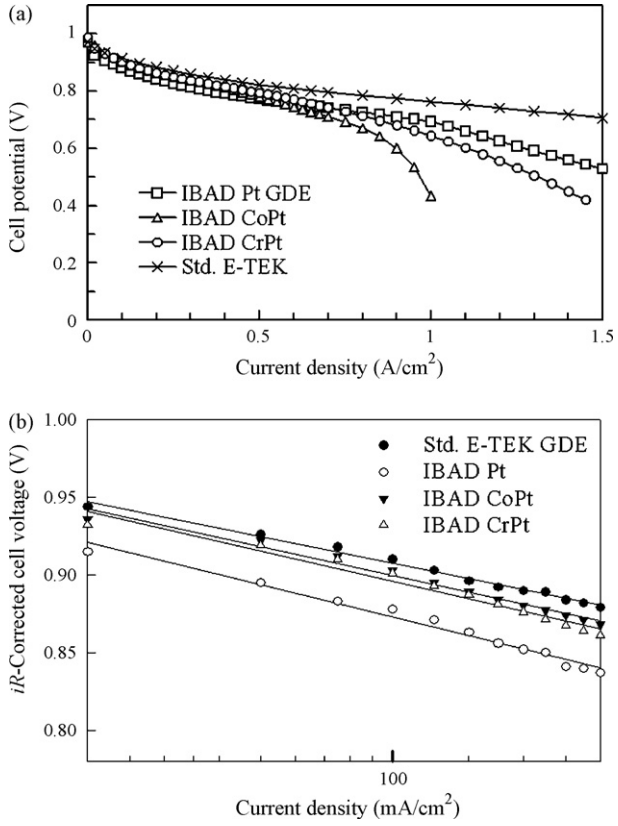

Fig. 3. Steady state polarization measured at 80 °C, 50/60 psig back-pressure (anode and cathode electrode respectively) for Pt/C (ETEK, 30% Pt on C, 0.5 mg/cm^2 loading and corresponding Pt and PtCo IBAD electrodes (550 Å deposit of the respective metal), corresponding to 0.08 mg/cm^2 loading for Pt. (a) Single cell polarization for all electrodes on a linear scale and (b) the corresponding Tafel plot of the cathode half cell polarization.

applications of PEMFC's laid by Gasteiger et al. [6] More details and quantitative analysis on fuel cell performance IBAD electrodes are available in previous publications [11,33–35].

3.3. Assignment of the absorption bands of ATR-IR Spectra of Nafion® 112 (H-form)

Infrared absorption studies, along with small angle X-ray, neutron scattering investigation and scanning probe microscopy imaging, have been used widely to elucidate the nanostructure of Nafion® membrane [52–54,64–66]. Fig. 4 and Table 2 indicate the assignment of various vibrational absorption bands, in the region between 900 and 1350 cm^{-1} wavenumbers as relevant to this study, associated with the chemical structure of Nafion® 112 membranes (DuPont Corp.) in H^+ form. The very strong absorption bands at 1142 and 1208 cm^{-1} wavenumbers correspond to the symmetric and asymmetric vibrations of $-CF_2$ groups in the hydrophobic fluorocarbon backbone, symmetric stretching of the sulfonate group is observed at 1059 cm^{-1}. The twin peak at 969 and 982 cm^{-1} is due to the presence of two ether linkages (–C–O–C–) in Nafion® side chain. Of the two ether vibration absorption bands in Nafion® membrane, the higher frequency band (i.e., the one at 982 cm^{-1}) is attributed to the ether linkage directly attached to the fluorocarbon backbone and is labeled as ether band 'B'. The corresponding lower frequency component at 969 cm^{-1} is labeled as ether band 'A', caused due to its proximity to the sulfonate group and its electron withdrawing character. This assignment of vibration absorption bands of ether linkages is based on prior work by Moore et al. [64] who contrasted the two ether absorption peaks in Nafion® against a single ether absorption band present in Dow perflourosulfonate ionomers (PFSI). Dow PFSI has only one ether linkage in its side chain and exhibits a single absorption peak centered at around ~969 cm^{-1}.

Table 2
Selective list of IR absorption peak assignments of H-Nafion® 112 as pertinent to this study in correspondence with Fig. 4.

Index	Wavenumber[a] (cm^{-1})	Peak assignments
(A)	969 m	υ_s(C–O–C), Ether band 'A', symmetric
(B)	982 m	υ_s(C–O–C), Ether band 'B', symmetric
(C)	1059 m	$\upsilon_s(SO_3^-)$, sulfonate group, symmetric
(D)	1142 vs	$\upsilon_s(CF_2)$, CF_2 group, symmetric
(D)	1208 vs. vb	$\upsilon_{as}(CF_2)$, CF_2 group, asymmetric
(E)	1303 sh	υ_s(C–C), symmetric

[a] Relative Intensity: m-medium; vs-very strong; vb-very broad; sh-shoulder.

Gierke et al. [67], proposed the ion-cluster network theory for the morphology of Nafion® membranes according to which the terminal sulfonate groups in the pendant side chains stretch out into approximately spherical clusters which also consists of sorbed water and hydrated cations, interconnected with each other by channels for ionic transport, and supported by hydrophobic fluorocarbon backbone material. Meanwhile, Yeager et al. [68] corroborated the conclusions of Falk et al. [69], that the ionic clusters are non-spherical in shape and have intrusions of side chain ether linkages, this was based on the three phase morphology for Nafion® consisting of the hydrophobic fluorocarbon phase, hydrophilic ionic clusters and an interfacial region between these two. This interfacial region is largely a void volume containing pendant side chain materials, a small amount of sorbed water and trace level of sulfonate exchange sites and counter ions. From the results of this present study, this interfacial region is of importance since they turn out to be the vulnerable site for radical species attack during fuel cell operation as discussed in the following sections.

3.4. Effect of radical-initiated degradation on membrane properties

Segmented cell durability tests were conducted to investigate the mechanism of degradation as a function of potential, temperature, and choice of electrocatalyst material as pertains to the operating cathode electrode environment. Prior publication [44–49] has suggested that one of the vulnerable locations for radical attack in a MEA is at the cathode (oxygen) side. This mechanism is based on the proposition of oxygen reduction reaction at the cathode of PEMFC proceeding via a parallel pathway where a two-electron reduction of oxygen occurs simultaneously with the formation of H_2O_2 intermediates [70] along with the predominant four electron reduction to H_2O; the peroxides then react with trace transition metals ions (Fe^{2+}, Cu^{2+}... found in membrane and/or carbon black catalysts support) to form radicals:

$$O_2 + 2H^+ + 2e^- \rightarrow H_2O_2 \quad (1)$$

$$M^{2+} + H_2O_2 \rightarrow M^{3+} + {}^{\bullet}OH + OH^- \quad (2)$$

$$M^{3+} + H_2O_2 \rightarrow M^{2+} + {}^{\bullet}OOH + H^+ \quad (3)$$

It has been pointed out that the metal ion and H_2O_2 concentrations necessary for the occurrence of hydroxyl radical can be very low (<10–25 mg L^{-1} H_2O_2 and 1 part Fe per 5–25 parts of H_2O_2 (wt/wt) [51]). Cathode operating potentials of 0.4, 0.6, 0.7 V vs. RHE were employed to study the influence of peroxide formation and subsequent membrane deterioration. Tests were conducted from room temperature to 80 °C to study the influence of temperature for various time periods ranging from 24 to 48 h. At the end of each durability test, the membrane was carefully separated from the electrode using a special procedure described earlier [37]. The changes in its proton conductivity (σ),

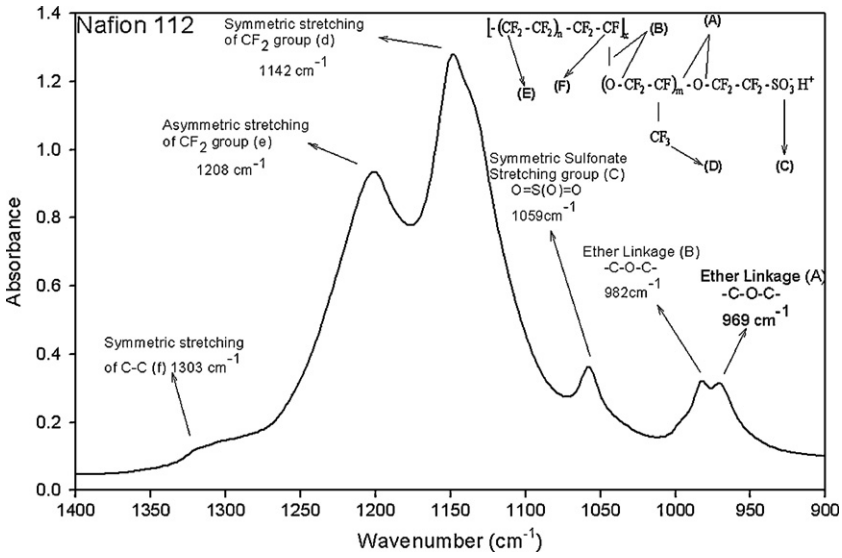

Fig. 4. ATR-IR Spectrum of Nafion® 112 (H-form) indicating absorption bands obtained using Mattson RS-2 FTIR instrument equipped with a pike MIRacle ATR unit with 45° ZnSe ATR Crystal. Also shown inside is the chemical structure of Nafion®.

Table 3
Basic membrane properties of pristine Nafion® 112 showing ion exchange capacity (η), membrane thickness, glass transition temperature (T_g), and proton conductivity (σ).

Membrane	Ion Exchange Capacity (η) [mEq g^{-1}]	Proton Conductivity (σ) [S cm^{-1} at 22 °C, 100% RH]	Thickness [mm]	Glass Transition Temperature, T_g [°C]
Nafion® 112	0.91	0.097	0.0508	140

ion exchange capacity (η) were determined and compared with that of non-degraded pure Nafion® membrane properties shown in Table 3, to estimate the extent of degradation quantitatively (Table 4). ATR-IR absorption spectra of degraded membranes were compared to spectra of pure membrane shown in Fig. 4 (obtained using Mattson RS-2 FTIR instrument equipped with a pike MIRacle ATR unit with 45° ZnSe ATR Crystal) to find the pathway of membrane degradation. ZnSe ATR crystal provides a penetration depth of 1.7–2 μm from the membrane surface in the IR wavenumber region of ~400–4000 cm^{-1}.

In an earlier publication detailed durability experiments conducted using our novel segmented cell assembly on various supported E-TEK Pt and Pt alloy electrocatalysts at the interface with Nafion® 112 membrane was reported [36]. This prior study involved a two pronged effort to elucidate (i) the correlation between peroxide generations measured at the ring electrode of a RRDE setup for a given electrocatalyst to that of the extent of membrane degradation observed in an operating fuel cell, and (ii) to elucidate the membrane degradation pathways at various fuel cell operating conditions triggered by peroxide formation. These experiments showed that there is a one-on-one correlation between peroxide yields observed at the ring electrode of a rotating ring-disk setup and extent of membrane degradation in an operating fuel cell for the same catalyst material. In the present investigation we attempt to use the same protocols and experimental design to compare the interfacial stability of conventional supported electrocatalysts with the IBAD Pt and PtCo samples. Briefly, these criteria include: 1) direct proportionality between peroxide generation at the cathode electrode/electrolyte interface of an operating fuel cell and extent of membrane degradation, 2) potential dependence of peroxide yield as observed in terms of progressively greater membrane degradation as a function of increased cathode operating potential up to 0.4 V vs. DHE.

Table 4
Effect of cathode side durability tests on IBAD electrodes subjected to a duration of 48 h at 50 °C using 30% Pt/C, IBAD 550 Pt, and IBAD 550 PtCo at a polarization potential of 0.4 V vs. DHE.

	% decrease in Conductivity	% decrease in Ion Exchange Capacity
ETEK-BASF 30% Pt/C	57	52
IBAD Pt/C	43	39
IBAD PtCo/C	49	49

Listed are the percentage decrease in proton conductivity σ (S cm^{-1}) and ion exchange capacity η (mEq g^{-1}).

Table 4 shows the loss in conductivity and ion exchange capacity of Nafion® after cathode side degradation test performed using three samples E-TEK-BASF Pt/C (conventional supported electrocatalyst), IBAD Pt and IBAD PtCo placed simultaneously in the same 5 electrode MEA in our segmented cell design and operated at 50 °C for 48 h and maintained at a constant potential of 0.4 V vs. DHE. Corresponding IR spectra of degraded membranes are shown in Fig. 5 and changes in the membrane properties in Table 4. As evident from these results, E-TEK Pt/C leads to higher degradation compared to IBAD Pt/C and IBAD PtCo/C electrodes. This is evident from the higher levels of membrane degradation (Fig. 5, IR data) and its consequent effect on membrane characteristics, loss in conductivity and ion exchange capacity (Table 4) as compared to the corresponding data from IBAD samples. Our previous effort [36] strongly indicates a one to one correlation of these cathodic interfacial membrane degradation to peroxide yield brought on as result of parallel $2e^-$ reduction of oxygen. This therefore serves as an indirect measure of peroxide generation on IBAD electrode, a parameter not measurable by standard RRDE electrode technique in contrast to conventional supported Pt or Pt alloy electrocatalysts. These results therefore indicate that peroxide yields on IBAD electrodes are possibly lower in magnitude compared to E-TEK Pt/C electrode. Fig. 5 shows that degradation is observed as sharp cleavage of side chain ether linkages associated with the membrane. This

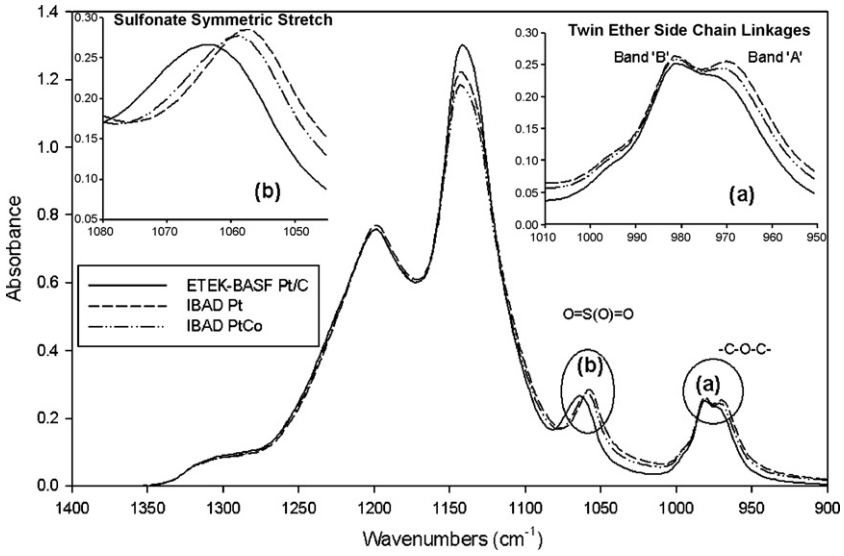

Fig. 5. IR Spectra of Nafion® 112 after cathode side degradation tests with three parallel samples of membranes at the interface with Pt/C and IBAD Pt and PtCo electrodes as indicated in the figure, operated for 48 h at 0.4 V (WE vs. DHE), 1 atm pressure and 50 °C conditions.

is estimated using relative changes in the peak intensities (absolute changes being unreliable due to inability of ridding the membrane of water completely). The spectra clearly indicates a preferential cleavage of ether band 'A' relative to ether band 'B'. This is discerned from the concomitant decrease in the intensity of peak at 969 cm^{-1} (ether band A) relative to peak at 982 cm^{-1} ether band B. The influence of cleavage of ether band 'A' is also seen on the relatively small decrease in intensity of sulfonate vibrational band at 1059 cm^{-1} the reason for this is discussed below. The relative changes in the intensity of ether bands A and B (Fig. 5) can be explained on the basis of ether linkage B (982 cm^{-1}) being directly attached to the fluorocarbon backbone and hence being relatively unaffected compared to the band at 969 cm^{-1}, indicating a preferential cleavage of the ether linkage directly attached to the sulfonate exchange groups. So, the loss in conductivity, shown in Table 4 is also due to preferential cleavage of ether band A in the side chain, because this cleavage subsequently scissions off the sulfonate ion exchange sites present at the terminal end of the pendant side chain and directly attached to ether band A. This preferential cleavage of ether band 'A' can also be rationalized by the fact that the presence of strong electron withdrawing groups in the fluorocarbon backbone stabilizes the ether band 'B' whereas the ether band 'A' in the side chain turns out to be relatively a more vulnerable region for peroxide radical attack. Also a very minor shift in the vibrational frequency of the sulfonate exchange sites to higher values is observed. Vibrational stretching frequency of sulfonate group in pure Nafion®-H form is localized in the spectral region around 1059 cm^{-1}. Sulfonate symmetric stretching of the degraded membranes is observed around 1062–1064 cm^{-1} and this is due to the modest contamination of membrane by counter ions (such as Na^+, Rb^+, Li^+, Cs^+, Ca^+), because minor cationic impurities from gas diffusion electrodes, humidification bottles, other fuel cell hardware are inevitable in the fuel cell operation. These foreign cations, usually have stronger affinity with the sulfonic acid group compared to H^+, and thereby replace the protons (H^+) attached to the sulfonate ion exchange sites; this replacement of protons by metal impurities causes a polarization of S-O dipoles and subsequently shifts sulfonate stretching to higher frequencies [52,64,71]. From the cathode catalyst perspective, it is concluded that IBAD Pt/C causes lowest level of degradation of the membrane compared to IBAD PtCo/C and E-TEK Pt/C (in ascending order). This could be a result of better transport properties of the IBAD electrodes, lower levels of peroxide yields and reduced levels of cationic impurities, etc. Also, shown in Table 5 is loss in conductivity of the membrane in contact with the three electrodes as a function of operating temperature of the fuel cell with each electrode individually maintained at 0.4 V vs. DHE for a period of 24 h. Similar decreases in ion exchange capacities of the degraded membranes are observed. It is seen that as the temperature increases there is an increase in the degradation level possibly due to increased peroxide yields at higher temperatures and more facile replacement of protons in the membranes by cationic impurities leading to peroxide initiated radical formation.

Following the discussions of Falk et al. [69] and Moore et al. [64] regarding the chemical nanostructure of Nafion® membrane briefly summarized above, it is likely that part of the side chain ether linkage intrudes into the hydrophilic ionic clusters. Consequently, during the period of cathode side degradation tests, it is observed that the radical species generated during the course of fuel cell operation initiates the polymer chain breakage by attacking the hydrophilic ionic cluster region (specifically the ether linkage intruding into the hydrophilic ionic cluster region) and virtually does not degrade the hydrophobic backbone of the membrane.

Table 5
Effect of cathode side durability tests on IBAD electrodes with O_2/N_2, 1 atm, for a duration of 24 h at various temperatures using 30% Pt/C, IBAD 550 Å Pt, and IBAD 550 Å PtCo at a polarization potential of 0.4 V vs. DHE.

Catalyst	Percentage decrease in Conductivity				Percentage decrease in Ion Exchange Capacity			
	@ RT	@ 40 °C	@ 60 °C	@ 80 °C	@ RT	@ 40 °C	@ 60 °C	@ 80 °C
ETEK-BASF	27%	34%	42%	51%	11%	26%	37%	46%
IBAD Pt	3%	3%	55%	84%	55%	2%	48%	85%
IBAD PtCo	19%	21%	72%	87%	16%	21%	66%	82%

Listed are the decrease in proton conductivity σ (S cm^{-1}) and ion exchange capacity η (mEq g^{-1}).

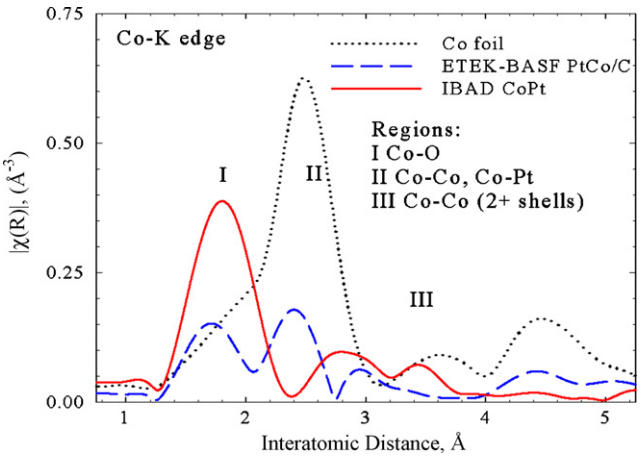

Fig. 6. Co-K edge (k^2 weighted, $2 < k < 15$ Å^{-1}, non-phase corrected) Fourier Transform EXAFS for IBAD Pt–Co (solid), *E-TEK* PtCo/C (dashed) and Co reference foil (dotted).

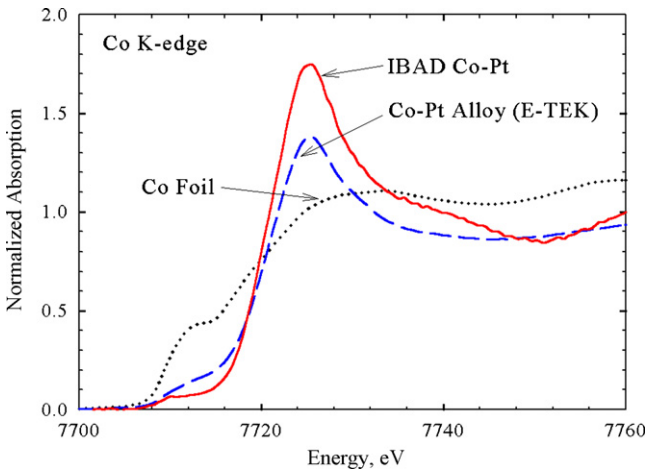

Fig. 7. XANES spectra taken at the Co-K edge for IBAD PtCo (solid), *E-TEK* PtCo/C (dashed) and Co reference foil (dotted).

4. XAS results and discussion

The Co-K edge Fourier Transformed EXAFS spectra are shown in Fig. 6 for both IBAD CoPt and standard *E-TEK* PtCo/C electrodes. The spectrum is broken down into three different regions with Region I, II and III representing the interactions between Co–O, Co–Co and Co–Pt, and higher coordination shells of Co–Co respectively. Both PtCo specimen studied exhibit a significant Co–O peak in region I. The IBAD electrode however, appears to be much more oxidized than the *E-TEK* PtCo alloy as evidenced by the larger peak in that region. It should also be noted that in Region II the IBAD electrode reveals a very low magnitude of Co–Pt interaction. This suggests that the Co is not well alloyed with the Pt which is also in accordance to cyclic voltammograms shown earlier. Also, the lack of Co–Co bonds indicates that Co predominantly exists as oxidized Co.

X-ray Absorption Near Edge Structure (XANES) for the above mentioned materials are presented in Fig. 7. It is evident from the XANES "white line" intensities that both CoPt samples are oxidized in comparison to the Co reference foil. The solid line representing the IBAD XANES has a much larger intensity centered on ~7724 eV in comparison to the standard CoPt alloy, in agreement with the FT-EXAFS in Fig. 6. The well defined XANES edge feature centered on ~7710 eV in the Co metal foil scan arise primarily from dipole allowed $1s \rightarrow 4p$ transition. In the case of the alloy electrodes (both E-TEK and IBAD) this XANES edge is absent and instead a weakly defined pre-edge feature is observed around ~7710 eV. This pre-edge feature is due to the dipole forbidden $1s \rightarrow 3d$ transition. This forbidden transition is made possible due to the hybridization of Co 3d orbital with that of the 2p electron states from oxygen. This hybridization causes the Co 3d orbital to assume *p-like* symmetry and makes possible the dipole forbidden $1s \rightarrow 3d$ transition [72,73]. This edge feature of the Co K-edge is also a proof of the fact that Co exists in its oxidized form in both the PtCo electrocatalysts. The minor difference between the pre-edge feature of E-TEK and IBAD PtCo electrodes can be explained by a possible charge transfer from Co to Pt in the case of E-TEK electrode due to alloying [74,75].

Fig. 8 contains *in situ* XANES spectra for the two materials taken at various fixed potentials. Again, it is evident that IBAD is oxidized to a greater extent; however progression towards more oxidizable potentials especially above 0.7 V vs. RHE indicates very little variation in the XANES intensities in the case of IBAD PtCo electrode, whereas the *E-TEK* PtCo alloy sample exhibits larger magnitudinal variance. It is expected that the white line intensity increases with electrode potential as the sample becomes oxidized. Since the IBAD sample is already highly oxidized, electrode polarization has little effect on the XANES at the potentials indicated, indicating thereby

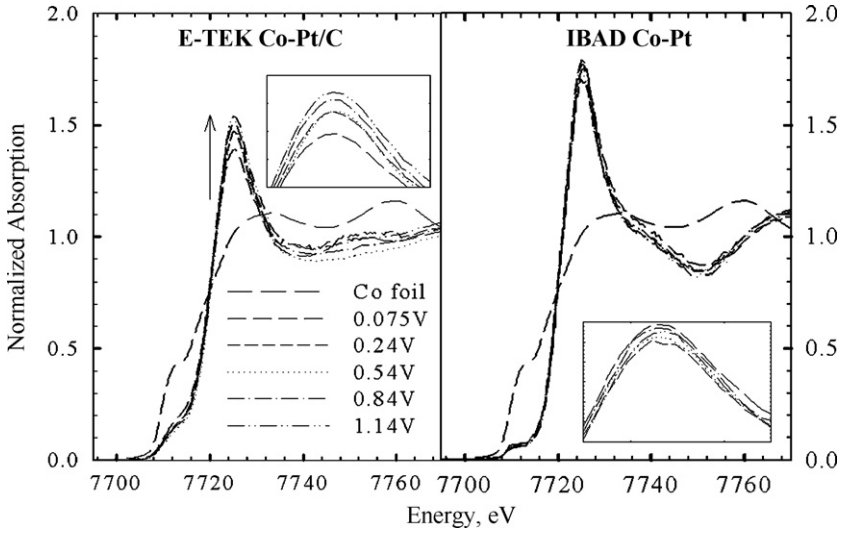

Fig. 8. *In situ* XANES spectra of *E-TEK* PtCo/C (left) and IBAD PtCo (right) taken at the potentials indicated (vs. RHE) in 1 M $HClO_4$.

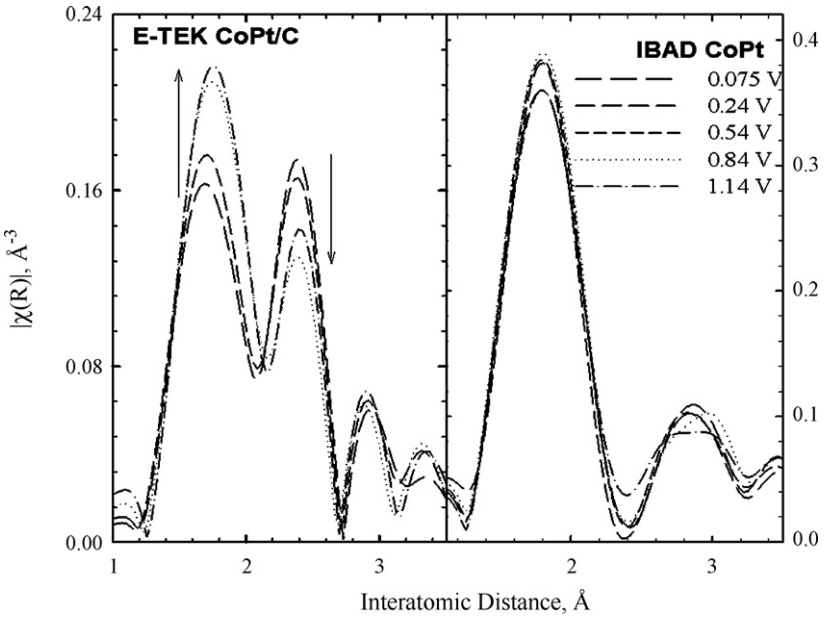

Fig. 9. *In Situ* EXAFS (k^2 weighted, $2 < k < 15$ Å^{-1}, non-phase corrected) spectra of *E-TEK* PtCo/C and IBAD PtCo at the electrode potentials indicated in Fig. 8.

that it remains completely passivated. The *E-TEK* sample does reveal an increase in white line amplitude, however, it never reaches the magnitude of the IBAD material because it is well alloyed with Pt and much of the Co is unavailable for oxidation.

In Situ FT-EXAFS of the above materials are presented in Fig. 9. Both materials exhibit similar line shapes and positions as in Fig. 6. The *E-TEK* material produces two peaks, one for Co–O and the other for Co–Pt/Co–Co, whereas the IBAD again produces a large peak in the Co–O region and only very small Co–Pt/Co–Co peak. Electrode polarization has a similar effect on the EXAFS as it has on the XANES. The *E-TEK* material undergoes rather large changes in the FT magnitude as the Co becomes oxidized. The Co–O peak near 1.8 Å increases with potential as the Co–Pt/Co–Co peak at 2.4 Å decreases, meaning CoO_x formation occurs at the expense of Co–Co/Co–Pt. The IBAD sample however, does not exhibit any appreciable change in FT magnitude. Again, this indicates that the IBAD Co is already oxidized to the maximum extent under these conditions and cannot be oxidized further. Interestingly, the Co from the IBAD sample does get reduced at low potentials of 0.075 V but only to a small degree. These *in situ* FT-EXAFS also indicate the remarkable stability of the Co in the unalloyed Co–Pt IBAD electrode as any dissolution would have manifested itself in the relative FT-intensities. This is a definitive evidence on the durability of these electrodes for application as ORR cathodes in a PEMFC.

5. Conclusions

Dual IBAD electrodes with mass manufacturability was prepared for targeted utilization as gas diffusion electrodes in PEMFC's leading to significant improvements in mass specific power densities obtained at ultra low noble metal loadings in contrast to commercially available state of the art Pt/C electrodes. Durability investigations at the electrode/electrolyte interface were performed using a novel accelerated technique from the perspective of peroxide initiated radical attack as a function of electrode materials, overpotential and temperature. Membrane degradation at the interface with IBAD Pt and PtCo electrode was found to be lower than standard state of the art Pt/C electrode, which is correlated qualitatively to peroxide initiated radical generation at the electrode/electrolyte interface as a result of the $2e^-$ pathway of the oxygen reduction reaction at the cathode side of an operating fuel cell. Also membrane degradation was found to be initiated by the peroxide radical attack at the side chain ether linkages connecting the ion exchange groups to the fluorocarbon backbone. Structure-property relationships between the IBAD electrodes obtained using *in situ* XAS experiments indicate that the Co present in IBAD Co–Pt alloy is highly oxidized and passivated and is not well-alloyed with Pt. With increasing operating potential Co present in E-TEK PtCo alloy shows an increasing tendency to get oxidized whereas Co present in IBAD Co–Pt does not since it is already heavily oxidized. *In situ* FT-EXAFS also indicates that the Co oxides in the PtCo IBAD electrodes are stable towards dissolution. Its main function appears to be as agents to improve the wettability and adherence of the Pt IBAD deposit over its layer.

Acknowledgments

The authors gratefully acknowledge the financial support from Army Research Office via a single investigator grant. The authors also acknowledge the financial support from Department of Energy, Basic Energy Sciences, for building and maintaining the National Synchrotron Light Source at Brookhaven National Laboratory, Upton, NY Contract No. DE-AC02-98CH10886.

References

[1] S. Srinivasan, R. Mosdale, P. Stevens, C. Yang, Annual Review of Energy and the Environment 24 (1999) 281.
[2] A.J. Appleby, Journal of Power Sources 37 (1992) 223.
[3] S.D. Fritts, R. Gopal, Journal of the Electrochemical Society 140 (1993) 3337.
[4] S.S. Penner (Ed.), Assessment of Research Needs for Advanced Fuel Cells, In: Energy (Oxford) 11(1–2) 1986.
[5] B.C.H. Steele, A. Heinzel, Nature (London, United Kingdom) 414 (2001) 345.
[6] H.A. Gasteiger, S.S. Kocha, B. Sompalli, F.T. Wagner, Applied Catalysis, B: Environmental 56 (2005) 9.
[7] S. Srinivasan, E.A. Ticianelli, C.R. Derouin, A. Redondo, Journal of Power Sources 22 (1988) 359.
[8] S. Srinivasan, Electrode Kinetic, Electrocatalytic Aspects of Electrochemical Energy Conversion 585 (1992).
[9] A.C. Ferreira, S. Srinivasan, Proceedings of the Electrochemical Society 94 (1994) 173.
[10] The Hydrogen Electrode Reaction and Electrooxidation of CO and H_2/CO Mixtures on Well Characterized Pt and Pt-Bimetallic Surfaces, Vol. 3, In: N.M. Markovic (Ed.), Wiley, Chichester, UK, 2003 (Chapter 26).
[11] M.S. Saha, A.F. Gulla, R.J. Allen, S. Mukerjee, Electrochimica Acta 51 (2006) 4680.
[12] M.S. Wilson, S. Gottesfeld, Journal of Applied Electrochemistry 22 (1992) 1.

[13] Y.-G. Chun, C.-S. Kim, D.-H. Peck, D.-R. Shin, Journal of Power Sources 71 (1998) 174.
[14] M.S. Wilson, S. Gottesfeld, Journal of the Electrochemical Society 139 (1992) L28.
[15] L. Xiong, A. Manthiram, Electrochimica Acta 50 (2005) 3200.
[16] Z. Qi, A. Kaufman, Journal of Power Sources 113 (2003) 37.
[17] M. Uchida, Y. Fukuoka, Y. Sugawara, H. Ohara, A. Ohta, Journal of the Electrochemical Society 145 (1998) 3708.
[18] J.C. Figueroa, Fabrication and use of electrodes and other fuel cell components having ultra low catalyst loadings coated thereon (E.I. Dupont de Nemours and Company, USA), Application: WO, 2005, 24 pp.
[19] T. Yamafuku, K. Totsuka, S. Hitomi, H. Yasuda, M. Yamachi, GS News Technical Report 63 (2004) 23.
[20] Z.-g. Shao, B.-l. Yi, J.-r. Yu, Dianhuaxue 6 (2000) 317.
[21] N. Tsumura, S. Hitomi, H. Yasuda, M. Yamachi, GS News Technical Report 62 (2003) 21.
[22] E.J. Taylor, E.B. Anderson, N.R.K. Vilambi, Journal of the Electrochemical Society 139 (1992) L45.
[23] E. Taylor, WO 2000028114, 2000.
[24] O. Antoine, R. Durand, Electrochemical and Solid-State Letters 4 (2001) A55.
[25] B.N. Popov, Plating and Surface Finishing 91 (2004) 40.
[26] S. Mukerjee, S. Srinivasan, A.J. Appleby, Electrochimica Acta 38 (1993) 1661.
[27] S. Hirano, J. Kim, S. Srinivasan, Electrochimica Acta 42 (1997) 1587.
[28] S.Y. Cha, W.M. Lee, Journal of the Electrochemical Society 146 (1999) 4055.
[29] C.K. Witham, W. Chun, T.I. Valdez, S.R. Narayanan, Electrochemical and Solid-State Letters 3 (2000) 497.
[30] J.K. Hirvonen, Materials Research Society Symposium Proceedings 792 (2004) 647.
[31] T. Hoshino, K. Watanabe, R. Kometani, T. Morita, K. Kanda, Y. Haruyama, T. Kaito, J. Fujita, M. Ishida, Y. Ochiai, S. Matsui, Journal of Vacuum Science & Technology, B: Microelectronics and Nanometer Structures–Processing, Measurement, and Phenomena 21 (2003) 2732.
[32] D.A. Kotov, Review of Scientific Instruments 75 (2004) 1934.
[33] A.F. Gulla, M.S. Saha, R.J. Allen, S. Mukerjee, Journal of the Electrochemical Society 153 (2006) A366.
[34] A.F. Gulla, M.S. Saha, R.J. Allen, S. Mukerjee, Electrochemical and Solid-State Letters 8 (2005) A504.
[35] M.S. Saha, A.F. Gulla, R.J. Allen, S. Mukerjee, ECS Transactions 1 (2006) 77.
[36] N. Ramaswamy, N. Hakim, S. Mukerjee, Electrochimica Acta 53 (2008) 3279.
[37] L. Zhang, S. Mukerjee, Journal of the Electrochemical Society 153 (2006) A1062.
[38] R.J. Allen, J.R. Giallombardo. Metal, metal oxide, and/or metal alloy thin-film formation on ion conductive polymer film by ion beam assisted deposition (De Nora S. p. A., Italy), Application: JP, 1998, 9 pp.
[39] C. Cavalca, J.H. Arps, M. Murthy, Fuel cell membrane electrode assemblies with improved power outputs and poison resistance (Gore Enterprise Holdings, Inc., USA). Application: WO, 2000, 125 pp.
[40] S. Srinivasan, Fuel Cells: From Fundamentals to Applications, Springer, New York, 2006.
[41] R. Liu, E.S. Smotkin, Journal of Electroanalytical Chemistry 535 (2002) 49.
[42] R.C. Urian, A.F. Gulla, S. Mukerjee, Journal of Electroanalytical Chemistry 554–555 (2003) 307.
[43] A. Parthasarathy, C.R. Martin, S. Srinivasan, Journal of the Electrochemical Society 138 (1991) 916.
[44] Q. Guo, P.N. Pintauro, H. Tang, A. O'Connor, Journal of Membrane Science 154 (1999) 175.
[45] M. Inaba, H. Yamada, J. Tokunaga, A. Tasaka, Electrochemical and Solid State Letters 7 (2004) A474.
[46] A.B. Laconti, M. Hamdan, R.C. McDonald, in: W. Vielstich, H.A. Gasteiger, A. Lamn (Eds.), Handbook of Fuel Cells-Fundamentals, Technology and Applications, vol. 3, John Wiley & Sons Ltd., New York, 2003, p. 647.
[47] A. Pozio, R.F. Silva, M. De Francesso, L. Giorgi, Electrochimica Acta 48 (2003) 1543.
[48] D.P. Wilkinson, J. St-Pierre, in: W. Vielstich, H.A. Gasteiger, A. Lamn (Eds.), Handbook of Fuel Cells - Fundamentals, Technology and Applications, vol. 3, John Wiley & Sons, Ltd., New York, 2003, p. 611.
[49] J. Yu, B. Yi, D. Xing, F. Liu, Z. Shao, Y. Fu, H. Zhang, Physical Chemistry Chemical Physics 3 (2003) 611.
[50] P. Maletzky, R. Bauer, J. Lahnsteiner, B. Pouresmael, Chemosphere 38 (1999) 2315.
[51] P. Maletzky, R. Bauer, J. Lahnsteiner, B. Pouresmael, Chemosphere 10 (1999) 2315.
[52] K.A. Mauritz, R.B. Moore, Chemical Reviews 104 (2004) 4535.
[53] C. Heitner-Wirguin, Journal of Membrane Science 120 (1996) 1.
[54] Z. Liang, W. Chen, J. Liu, S. Wang, Z. Zhou, W. Li, G. Sun, Q. Xin, Journal of Membrane Science 233 (2004) 39.
[55] F.N. Buchi, B. Gupta, O. Haas, G.G. Scherer, Electrochimica Acta 40 (1995) 345.
[56] H. Gunzler, H.-U. Gremlich, IR Spectroscopy An Introduction, Wiley-VCH, Cambridge, 2002.
[57] C. Ma, L. Zhang, S. Mukerjee, D. Ofer, B. Nair, Journal of Membrane Science 219 (2003) 123.
[58] J. McBreen, W.E. O'Grady, K.I. Pandya, R.W. Hoffman, D.E. Sayers, Langmuir 3 (1987) 428.
[59] M.A. Enayetullah, T.D. DeVilbiss, J.O.M. Bockris, Journal of the Electrochemical Society 136 (1989) 3369.
[60] M. Newville, Journal of Synchrotron Radiation 8 (2001) 322.
[61] M. Newville, P. Livins, Y. Yacoby, E.A. Stern, J.J. Rehr, Journal of Physical Review B 61 (1993) 13144.
[62] S.S. Abd El Rehim, A.A. El Basosi, S.M. El Zein, M.M. Osman, Collection of Czechoslovak Chemical Communications 59 (1994) 2383.
[63] M. Pourbaix, Atlas of Electrochemical Equilibria in Aqueous Solutions, Pergamon Press, New York, 1996.
[64] K.M. Cable, K.A. Mauritz, R.B. Moore, Journal of Polymer Science: Part B: Polymer Physics 33 (1995) 1065.
[65] A. Gruger, A. Regis, T. Schmatko, P. Colomban, Vibrational Spectroscopy 26 (2001) 215.
[66] C. Heitner-Wirguin, Polymer 20 (1979) 371.
[67] W.Y. Hsu, T.D. Gierke, Journal of Membrane Science 13 (1983) 307.
[68] H.L. Yeager, A. Steck, Journal of the Electrochemical Society 128 (1981) 1880.
[69] M. Falk, Canadian Journal of Chemistry 58 (1980) 1495.
[70] E. Yeager, Electrochimica Acta 29 (1984) 1527.
[71] A. Eisenberg, H.L. Yeager, Perfluorinated Ionomer Membranes, American Chemical Society, Washington, DC, 1982.
[72] L.A. Grunes, Physical Review B: Condensed Matter and Materials Physics 27 (1983) 2111.
[73] P. Behrens, TrAC, Trends in Analytical Chemistry 11 (1992) 237.
[74] E.K. Hlil, R. Baudoing-Savois, B. Moraweck, A.J. Renouprez, Journal of Physical Chemistry 100 (1996) 3102.
[75] S. Mukerjee, S. Srinivasan, M.P. Soriaga, Journal of the Electrochemical Society 142 (1995) 1409.